Charge order, frustration relief, and spin-orbit coupling in U₃O₈

Rolando Saniz [*]

CMT & NANOlab Center of Excellence, Department of Physics, University of Antwerp, B-2020 Antwerp, Belgium

Gianguido Baldinozzi [†]

Université Paris-Saclay, CentraleSupélec, CNRS, SPMS, F-91190 Gif-sur-Yvette, France

Ine Arts and Dirk Lamoen

EMAT & NANOlab Center of Excellence, Department of Physics, University of Antwerp, B-2020 Antwerp, Belgium

Gregory Leinders and Marc Verwerft

Belgian Nuclear Research Centre (SCK CEN), Institute for Nuclear Materials Science, B-2400 Mol, Belgium

Research efforts on the description of the low-temperature magnetic order and electronic properties of U₃O₈ have been inconclusive so far. Reinterpreting neutron scattering results, we use group representation theory to show that the ground state presents collinear out-of-plane magnetic moments, with antiferromagnetic coupling both in-layer and between layers. Charge order relieves the initial geometric frustration, generating a slightly distorted honeycomb sublattice with Néel-type order. The precise knowledge of the characteristics of this magnetic ground state is then used to explain the fine features of the band gap. In this system, spin-orbit coupling (SOC) is of critical importance, as it strongly affects the electronic structure, narrowing the gap by ∼38%, compared to calculations neglecting SOC. The predicted electronic structure actually explains the salient features of recent optical absorption measurements, further demonstrating the excellent agreement between the calculated ground state properties and experiment.

I. INTRODUCTION

The actinide element uranium is the main component of nuclear fuels, being most commonly applied in the form of the binary oxide uranium dioxide (UO₂) or as an alloyed metal. These compounds are very susceptible to oxidation and their resulting physicochemical properties have been investigated extensively over the past decades [1–4]. Particular focus has been given to the solid-state transformations occurring due to oxidation, which result in the formation of mixed-valence uranium oxides such as U₃O₇ and U₃O₈ [5–10]. From an application point of view, this interest relates mainly to the safe and sustainable management of nuclear fuel during fabrication, handling, and storage or disposal. Additionally, there has been a more fundamental interest to understand the properties and behavior of actinide compounds, owing to peculiar electronic interactions between $5f$ and $6d$ orbitals and the states of neighboring atoms [11–13].

The room-temperature crystal structure of U₃O₈ was determined with good accuracy by Loopstra in 1964 [14], and electrical conductivity measurements demonstrated the semiconductor nature of U₃O₈ around the same time [15]. However, no measurements of the band gap were reported at that time. Only during the past decade have experimental

researchers started studying pointedly the electronic structure and the magnetic properties of U₃O₈. There are now several reports of measurements using spectroscopy techniques to assess the chemical state of the uranium atoms, and of the band gap [12,16–20]. Furthermore, from the theoretical point of view, various studies using first-principles methods have been published [20–24].

U₃O₈ is a system that stands out among oxide systems because of the expected anisotropic character of the magnetic interactions. Indeed, the crystal structure is layered, charge localization is expected to occur, and magnetic moments are localized onto an almost undistorted underlying triangular lattice. Interactions among layers produce strong anisotropic effects generated by including further neighbors or using a different exchange coupling [25,26]. Therefore, in this quasi-two-dimensional system, the display of long-range magnetic correlations is expected. The question of the description of the actual magnetic correlations in U₃O₈ at low temperature has been addressed in two recent research papers [24,27]. Neutron scattering was used to investigate magnetic order at low temperature, and the results provided irrefutable evidence of magnetic superlattice reflections below 25 K. The phase correlates with a heat capacity anomaly [28] and a magnetic susceptibility peak [29]. This supports the onset of an antiferromagnetic (AFM) order below $T_N \approx 25$ K. Following the experimental evidence, electronic structure calculations using density function theory (DFT) were used to determine their respective energies [24]. However, to confidently assign the

---
[*]rolando.saniz@uantwerpen.be
[†]gianguido.baldinozzi@centralesupelec.fr

ground state, all possible arrangements should be evaluated, which becomes an enormous effort if the magnetic symmetry restrictions are not taken into account.

In this paper we adopt an approach based on group representation theory to settle the matter of the ground state of U_3O_8. We compare the results of theory with DFT-based calculations and with the experimental evidence, predicting systematic absences of magnetic reflections, and using this feedback to determine the unique model that explains the experimental observations. Then we discuss the implications of this model of anisotropic interactions among magnetic moments, that can be described by a generalized AFM Heisenberg spin Hamiltonian with in-layer intersite anisotropic interactions between a ring of six spins, while on-site interactions are responsible for a direct superexchange mechanism mediated by the p_x orbital of the O atoms bridging the layers. We find that, in the ground state, the frustration of magnetic moments is lifted by charge order, producing a classical Néel-type AFM state where the nearest-neighbor magnetic moments (intralayer, but also interlayer) display an antiferromagnetic coupling. The precise knowledge of the characteristics of this magnetic ground state is then used to evaluate the uranium chemical state by Hirshfeld and Bader charge analysis, and to explain the fine features of the band gap.

II. COMPUTATIONAL METHOD

We performed our calculations with the VASP code [30], using the projector augmented-wave method (PAW) [31]. The PAWs for oxygen and uranium counted 6 and 14 valence electrons, respectively ($6s^2 6p^6 5f^3 6d^1 7s^2$, for the latter). The exchange-correlation interactions were described within the Perdew-Burke-Ernzerhof approximation and including a Hubbard U term to describe the on-site repulsion between U $5f$ electrons (PBE $+ U$), as applied by Dudarev *et al.* [32], using $U_{eff} = U - J = 3.96$ eV, as in that seminal work. The energy cutoff was set to 600 eV, energies were converged to within 10^{-6} eV, and forces to 0.03 eV/Å. As mentioned above, spin-orbit coupling (SOC) was taken into account in all our calculations because of its important effect on the electronic properties in other uranium oxide systems: For instance, calculations neglecting SOC yield incorrect U $5f$ occupancies in U_3O_7, incorrectly predicting a metal instead of a semiconductor character [33]. We also performed a GW calculation to benchmark our PBE $+ U$ results [34]. We applied the partially self-consistent quasiparticle approximation to GW (QPGW_0), which uses the spectral method to iterate the Green's function and includes the nondiagonal components of the self-energy, as implemented in VASP [35]. The dielectric function was calculated using a $9 \times 14 \times 14$ **k**-point mesh. The complex shift η for the Kramers-Kronig calculation was set at 0.02 [36].

III. RESULTS AND DISCUSSION

A. Symmetry analysis of the possible magnetic ground state

The symmetry group describing the crystal structure of the room- and low-temperature phase of U_3O_8 is *Amm*2 (No. 38), with reported lattice parameters of $a = 4.14(8)$ Å, $b = 11.96(6)$ Å, and $c = 6.71(7)$ Å [14] (note that a C-centered orthorhombic cell can be equivalently used; see

Ref. [37]). The U atoms are coordinated with seven oxygen atoms, forming edge-sharing UO_7 pentagonal bipyramids. The O atoms forming the pentagons and the U atom sit in a plane, forming a stack of dense layers bridged by the apical O atoms of the bipyramids (see Fig. S1 in the Supplemental Material [38]). In this structure, there are two independent U atoms, U1 (Wyckoff position 2*a*) and U2 (Wyckoff position 4*d*), associated to formal U^{6+} and U^{5+}, respectively [17,18]. Miskowiec *et al.* [27] report the appearance of superlattice reflections below T_N that can be generically indexed as $(\frac{1}{2}kl)$. This observation implies that the magnetic unit cell is twice the size of the crystallographic unit cell along the direction of the *a* lattice parameter. The uranium magnetic moments display a collective antiferromagnetic order below T_N which, as in UO_2, can be represented in terms of quantized spin waves (magnons). Below T_N, the magnetic order can be described by a magnetic irreducible representation at the $\mathbf{q}_Z = (\frac{1}{2}00)$ point of the Brillouin zone of the nonmagnetic phase (for further remarks on this, see Sec. II in the Supplemental Material [38]). It is worth mentioning that several magnetic reflections of the type $(\frac{1}{2}0l)$ are extinct, a key piece of information for the final choice of the magnetic space group. The magnetic irreducible representations at $\mathbf{q}_Z$ allow the determination of the complete set of compatible magnetic structures that can be used to simulate the scattered intensities of a neutron diffraction experiment. We add that the spin waves can couple with a zone center phonon of symmetry A_1 producing a static distortion of the structure.

There are only four possible magnetic configurations of magnetic moments localized at U atom positions that generate magnetic reflections of the type $(\frac{1}{2}kl)$. Each configuration belongs to a different magnetic irreducible representation ($\Gamma_{mag} = mZ_1 \oplus 3mZ_2 \oplus 3mZ_3 \oplus 2mZ_4$). Two of these configurations involve collinear magnetic moments along the *x* axis, the direction normal to the dense layers (all magnetic moments have $m_y = m_z = 0$): The magnetic space group induced by the mZ_1 irreducible magnetic representation is $A_{2a}mm2$ (OG No. 38.6.270 according to the Opechowski-Guccione (OG) convention and Litvin's notation [39]) and the one induced by mZ_4 is the magnetic space group $A_{2a}mm'2'$ (OG No. 38.9.273). The two other configurations involve a noncollinear arrangement of the magnetic moments that align in the *yz* plane (all magnetic moments have $m_x = 0$). The mZ_2 magnetic irreducible representation gives the magnetic space group $A_{2a}mm'2'$ [OG No. 38.9.273, origin shifted by $(\frac{1}{2}00)$], while mZ_3 gives the magnetic space group $A_{2a}mm2$ [OG No. 38.6.270, origin shifted by $(\frac{1}{2}00)$]. These four configurations are the only ones compatible with the experiment and their specific arrangements of the magnetic moments are directly responsible for different intensities of the predicted magnetic reflections. They are depicted in Fig. 1.

Only the magnetic arrangement induced by the mZ_1 irreducible representation produces the correct set of systematic extinctions for the $(\frac{1}{2}0l)$ magnetic reflections compatible with the experiment. The corresponding magnetic structure displays interesting features: First, the A_{2a} magnetic centring operator requires a stack of two layers of bipyramids UO_7 to describe the structure, effectively doubling the lattice along the *x* direction. Interestingly, the magnetic symmetry induced by the mZ_1 irreducible representation forbids magnetic
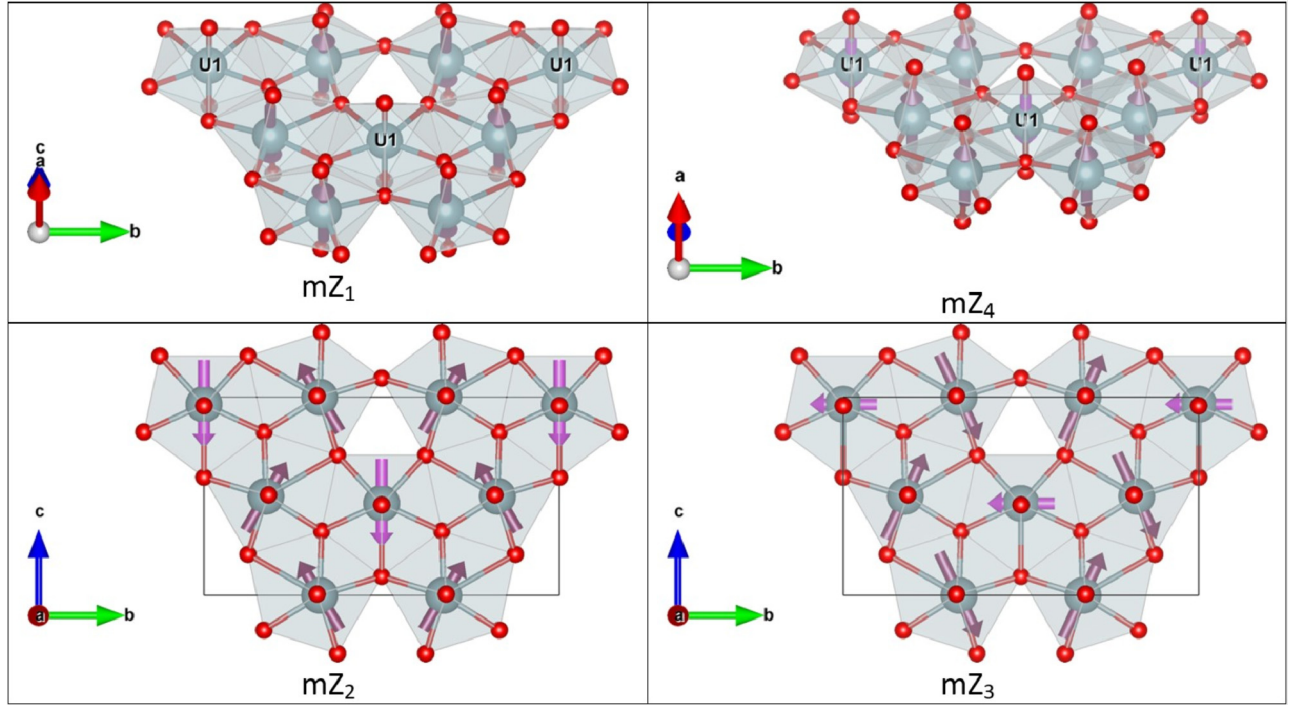
FIG. 1. The schematic figures above display the characteristic ordering of the magnetic moments of U atoms within each one of the four possible structures. Only one of the two layers composing the magnetic structure is represented. In the next layer magnetic moments are always flipped.

moment localization at U1. This correlates favorably with the hypothesis that U1 atoms have a 6+ oxidation state [17]. Note that the magnetic structure induced by the other irreducible representations would in principle permit magnetic moments on U1. Moreover, symmetry constrains the magnetic moments of nearest-neighbor U2 atoms of a same layer in an AFM configuration without breaking the A centering or changing the (x, y) unit cell dimension and, moving along x from one layer to the next, the magnetic moments of the the U2 atoms also display an AFM coupling [see Fig. S1(d) in the Supplemental Material [38]]. The low $\mathbf{q}$ magnetic reflections predicted by the mZ_1 AFM model are listed in Table I.

TABLE I. Low $\mathbf{q}$ magnetic reflections predicted by the mZ_1 AFM model.

HKL	q (Å^{-1})	Model prediction	Miskowiec [27]
(100)	0.76	Extinct	Absent
(110)	0.92	Extinct	Absent
(101)	1.20	Extinct	Absent
(120)	1.29	Extinct	Absent
(111)	1.31	"Strong"	Observed
(121)	1.60	Extinct	Absent
(130)	1.75	Extinct	Absent
(131)	1.98	Very weak	Quite weak
(102)	2.02	Extinct	Absent
(112)	2.09	Extinct	Absent
(140)	2.23	Extinct	Absent
(300)	2.27	Extinct	Absent
(122)	2.28	Very weak	Observed
(310)	2.33	Extinct	Absent

Actually, the mZ_1 configuration corresponds to the one with smaller energy among those analyzed in the set of DFT calculations in Ref. [24]. Unfortunately, that set does not include the three other configurations that are also predicted for magnetic instabilities at $\mathbf{q}_Z$ and that are candidates to represent excited configurations of the ground state. Our calculations provide slightly higher energies for these alternative models; actually, the mZ_3 configuration seems unstable and it converges to a configuration equivalent to the one induced by mZ_2. To summarize, $A_{2a}mm2$ is the space group of the ground state of U$_3$O$_8$ compatible with the experimental evidence and it corresponds to a stack of two opposite Néel-type magnetic states where all U2 magnetic moments in the next layer systematically flip along x, and where the U2 atoms within a same layer form a six-spin ring of alternating ordered AFM moments. This is illustrated in Fig. 2, where we show the calculated magnetization density m_x. The gold (cyan) color indicates that the magnetic moment is in the positive (negative) direction. Figure 2(a) displays a top view of the unit cell, clearly showing that the magnetic moments arrange to form a honeycomb lattice with Néel-type AFM order. We note that the magnetic moments are quite localized. The magnetization isosurfaces shown correspond to a value of only 5% of the maximum value. The bonding between U2 atoms is asymmetric in the in-plane directions, suggesting an effective coupling of the magnetic instability with the Γ_1 phonons. Figure 2(b) shows a side view, exhibiting the interlayer AFM coupling.

B. Electronic structure: Spin-orbit coupling and charge ordering

The electronic density of states was reported in Ref. [24], following a DFT $+ U$ approach including SOC. Our results
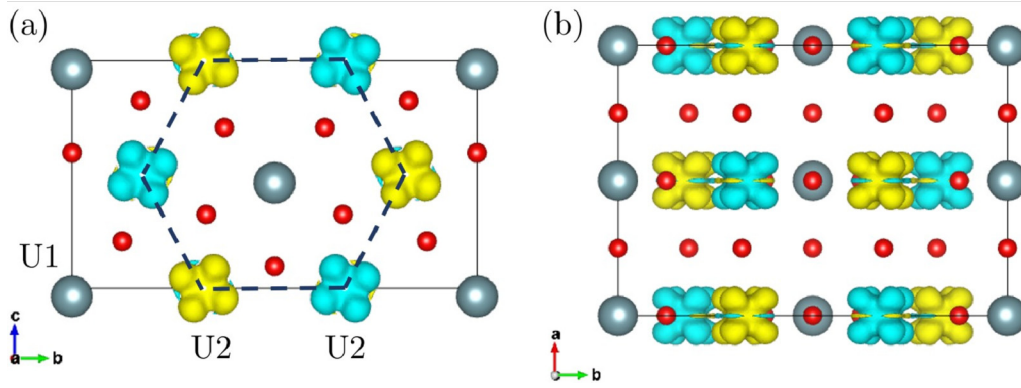
FIG. 2. Magnetization density along the direction of the *a* axis. Gold indicates a positive magnetization and cyan a negative one. (a) Top view of the orthorhombic unit cell. This shows the in-plane honeycomb Néel-type AFM order. (b) Side view of the unit cell, showing the interlayer AFM coupling. This strongly suggests a type of superexchange mechanism mediated by the oxygen atoms between the U2 atoms.

agree qualitatively; see the bands and density of states plots in Sec. III in the Supplemental Material [38]. We just note here that our band gap value is 1.27 eV, and that the spin and orbital magnetic moments of the U2 atoms are $\pm 0.90\,\mu_B$ and $\mp 1.17\mu_B$, respectively [40]. It is important to recognize that there is a notable cooperative effect between charge localization and SOC. Without charge order, i.e., without the electron correlation provided by the Hubbard U, U_3O_8 is predicted to be a metal, with the manifold of $5f$ states of the U1 and U2 atoms quasidegenerate in energy. Localization splits the the U1 and U2 atoms f states around the Fermi level, allowing the opening of the gap, with the U2 f states dominating the upper valence band and the U1 f the lower conduction band. Therefore, a finite U value is required to drive the system into the AFM phase: From a fundamental point of view, this might have interesting consequences in substituted systems as tuning the Hubbard value can lead to critical properties. Moreover, minimal seeds of $\pm 0.01\mu_B$ are sufficient to obtain the correct AFM order and correct magnetic moments. On the other hand, SOC acts to strongly lower the cost of occupying the U1 states in the conduction band, thus reducing significantly the band gap. This is illustrated in the upper panel in Fig. 3, where we compare the total density of states of a calculation including SOC and a calculation neglecting it (with the same magnetic moment configuration). In the latter case the band gap widens to 2.05 eV, a dramatic change from the 1.27 eV of the SOC calculation. Such a giant SOC effect on the conduction band has been reported in other systems, such as hybrid perovskites [42]. Moreover, the amplitude of the magnetic moment of the U2 atoms is strongly affected by SOC, as they are estimated to be $1.13\mu_B$, i.e., $\sim 26\%$ larger, when SOC is neglected (for a further analysis of the effect of SOC on the U $6p$ and $5f$ projected densities of states, see Sec. IV in the Supplemental Material [38]).

To gauge the band gap value obtained with a PBE+U+SOC calculation, we considered a more accurate approach. As already indicated, for this purpose we performed a partially self-consistent quasiparticle QPGW_0 calculation, including SOC. In this approach the self-energy (i.e., exchange and correlation) is described in a more fundamental way, yielding band gap values much closer to experiment

[35]. Our QPGW_0 calculation gives a band gap value of ~ 1.20 eV, only $\sim 6\%$ below the PBE + U + SOC result. We judge that this finding strongly supports the quality and
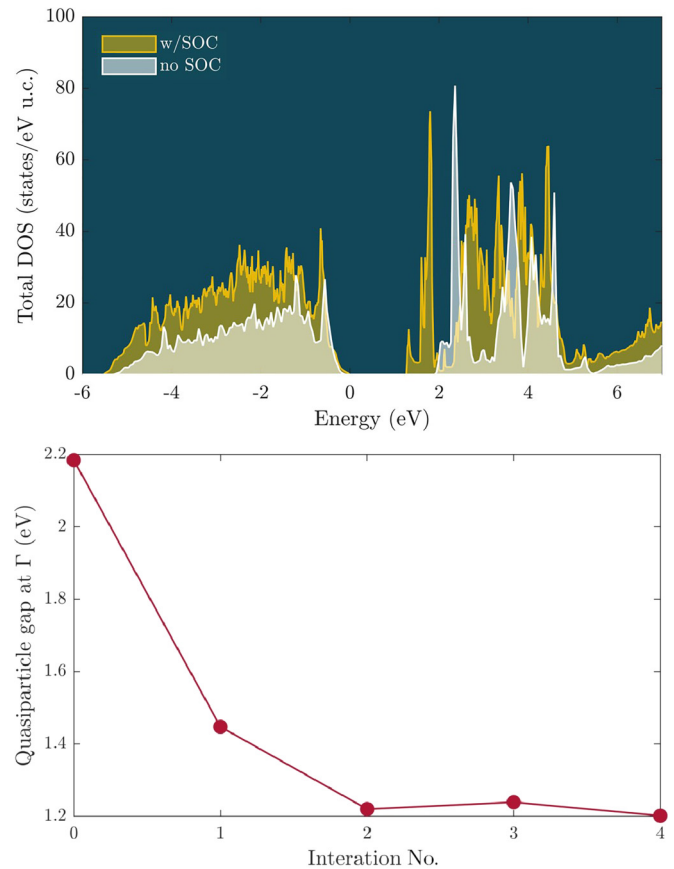

FIG. 3. Upper panel: Comparison of the total density of states calculations with and without including spin-orbit coupling. The absence of the latter leads to considerable energy shifts, affecting binding energies and especially the conduction band, resulting in a band gap of 2.05 eV. Lower panel: Convergence of the QPGW_0 band gap value at Γ with iteration number. Convergence is typically achieved in four iterations (see Ref. [41]).

TABLE II. Calculated U atom charge states.

U atom	Formal charge	Hirshfeld-I	Bader[a]
U1	6+	4.144	3.068
U2	5+	3.723	2.910

[a]Bader charge state: No. valence e − Bader charge.

robustness of our results. The small difference could be an indication that the Hubbard U electronic screening correction value used in our calculation is slightly larger than what is optimally required for U_3O_8. Be that as it may, a slightly lower U value would have no significant qualitative impact on our results, bringing only small quantitative changes. In the lower panel of Fig. 3 we show the rapid convergence of the QPQW_0 band gap value with iteration number.

A decomposition of the charge density in an extended solid can be performed by atoms-in-molecules (AIM) methods that have the advantage of providing a sum rule for the expectation values of the charge obtained by a topological partition of the whole system [43]. Two methods provide a good correlation between the quantum mechanical charge density and the qualitative concepts of atomic charge: the iterative Hirshfeld method (Hirshfeld-I) and the Bader charge analysis. The Hirshfeld-I method is based on sharing the charge density at each point in space among the surrounding atoms in proportion to a reference density at the corresponding distances from the nuclei [44]. In the Bader charge analysis the charge is divided among atoms by what are called zero-flux surfaces in the three-dimensional (3D) charge density [45]. Results of both methods are reported in Table II. The higher value associated to the U1 atomic site indicates this site has a higher formal valence state as compared to the atomic site U2, as is expected from experimental evidence [17]. Furthermore, the values assigned from the Bader charge analysis agree well with reported values for U^{6+} (3.070) and U^{5+} (2.965) in U_3O_8

[46]. Similarly, the Hirshfeld-I charge values are in agreement with those in U^{6+} and U^{5+} environments reported recently in the related structure of U_3O_7 [33].

C. Proposed superexchange coupling mechanism between U2 atoms in adjacent layers

We posit that the AFM coupling between U2 atoms across layers can be understood in terms of the 180° cation-anion-cation superexchange mechanism advanced by Anderson, Kanamori, and Goodenough in the 1950s (see Refs. [47–49]). A precise discussion of the mechanism is complicated by the fact that spin is no longer a good quantum number because of SOC. However, SOC can be reasonably ignored in a qualitative discussion of the mechanism. First, we point out that the approximate point group of the U2 atoms is $C5v$. The crystal field splits the f orbitals into states belonging to four irreducible representations of the approximate point symmetry group $C5v$: A_1, E_1, $E_2(1)$, and $E_2(2)$, as shown in Fig. 4. The $E_2(1)$ states have the lowest energy, while the nondegenerate A_1 state has the highest energy, represented by the f_{x^3} spherical harmonic base function. Using Anderson's terminology [47], in the "ionic configuration" the U2 ions have a formal 5+ valence state and the bridging O ion a 2− valence state. The U2 ions are in their high spin state, while the O ion has zero spin. In the superexchange mechanism, an electron from the O ion is excited via a virtual process to an empty state in one of the U2 ions. Here, this can occur because the A_1 f_{x^3} orbital overlaps with the O p_x orbital, and, following Hund's rule, the virtual electron maximizes the total spin virtual configuration of U2. At the same time, the other electron of the $O^−$ ion, which has opposite spin, couples ferromagnetically to the other U^{5+} ion [because the p_x orbital is orthogonal to the states belonging to $E_2(1)$]. This mechanism can explain the resulting AFM U2-U2 coupling across layers. The in-plane AFM coupling is simpler and may be described by a traditional anisotropic Heisenberg Hamiltonian. Similar
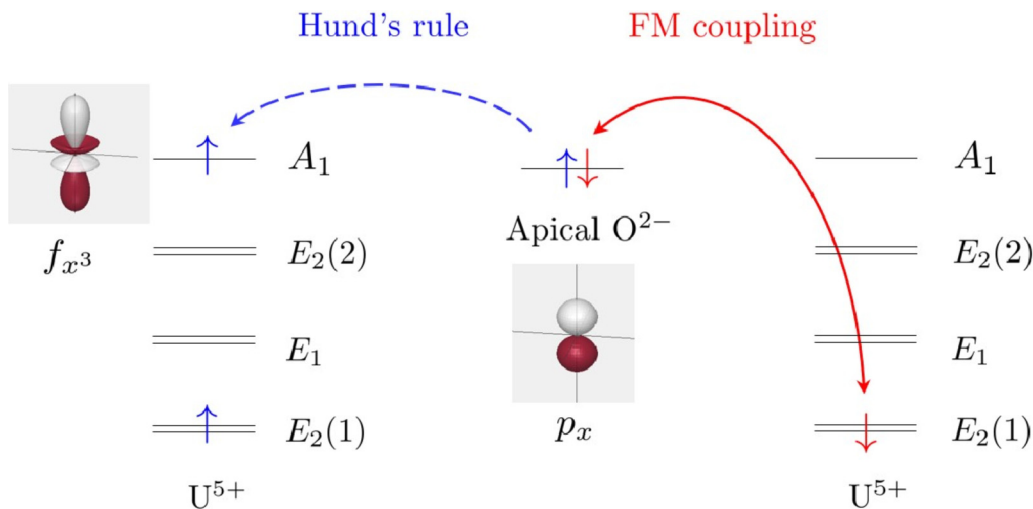

FIG. 4. Illustration of the Anderson-Goodenough-Kanamori rule for AFM superexchange coupling in the 180° U2-O-U2 configuration. Owing to orbital overlap, an oxygen ion electron is virtually excited to a neighboring U2 ion, with a spin complying to Hund's maximum spin rule. The unpaired electron on the $O^−$ ion, which has opposite spin, couples ferromagnetically to the other U2 ion. This is because the p_x orbital is orthogonal to the $E_2(1)$ states. The effective U2-U2 coupling is AFM.
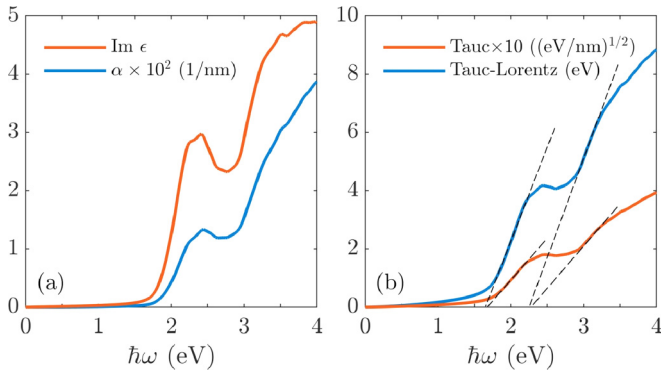
FIG. 5. (a) Imaginary part of the dielectric function and absorption coefficient of U_3O_8. (b) Tauc and Tauc-Lorentz plots, often used in experiment to determine indirect band gap values. As explained in the main text, in the present case the linear extrapolations to the abscissa (represented by the dashed lines) lead to values not directly related to the band gap in U_3O_8.

anisotropic couplings, generating a very rich phenomenology, were seen in other systems [25,26].

D. Optical absorption and band gap

To provide a further comparison with experiment, we calculated the dielectric function and absorption coefficient of U_3O_8. As can be expected, U_3O_8 is optically anisotropic, close to uniaxial. We considered thus the isotropic averages (i.e., one third of the trace of the tensors), which can be directly compared with data from a polycrystalline sample (for more details on the calculations, see Sec. V in the Supplemental Material [38]). We use the report of He and co-workers [16] as a benchmark, as it is more detailed than other studies [19,20]. We assert that our results explain the reasons for the specific structural features observed in the absorption spectrum. In Fig. 5(a) we present plots of the imaginary part of the dielectric function and of the absorption coefficient. Absorption starts to develop only as energies approach ~2 eV, clearly indicating that the joint density of states at lower energies is nearly negligible. After a dip around ~2.7 eV, a second strong increase in absorption develops around ~3 eV. These features are readily interpreted as arising from U2 to U1 transitions [see the projected densities of states in Fig. S2(b)]. For comparison with Ref. [16], in Fig. 5(b) we present the plots of two types of Tauc plots. Such plots are often used in experiment to interpret absorption spectra. Typically, the absorption edge

is assumed to indicate the value of the fundamental band gap. The plots presented in Ref. [16] are remarkably close to ours, regarding both the absorption coefficient and the Tauc extrapolations [50]. From the extrapolations, He and co-workers deduce that their sample would contain a mix of U_3O_8 and UO_3, with the lower absorption edge indicating the band gap of U_3O_8 and the one above the band gap of UO_3 [51]. As our calculation shows, however, the lower absorption edge does not indicate the band gap value of U_3O_8. Indeed, the density of states at the top of the valence band is too low to result in a significant absorption. It is the strong increase of the density of states at energies approaching 0.6 eV below the valence band that gives rise to the sharp increase in the absorption (peaking just above 2 eV). The linear extrapolations only indicate at what energy this apparent absorption onset begins. Thus, the conclusion in Ref. [16] that the band gap of U_3O_8 falls between 1.67 and 1.81 eV appears to be due to a misinterpretation of the Tauc plots they analyze [52].

IV. CONCLUSIONS

In this work, starting from neutron scattering data, we use group representation theory to irrefutably determine the ground state magnetic order in U_3O_8. First-principles methods were subsequently used to show that the low-temperature phase of U_3O_8 has the configuration of a Néel state, with simultaneous in-layer and interlayer AFM coupling. The in-layer geometric frustration is relieved by charge localization. In this system, SOC is of critical importance, and it was found to strongly affect the states of the conduction band, narrowing the gap by ~38% compared to calculations neglecting it. The predicted electronic structure explains the salient features observed in optical absorption measurements and it provides an excellent match between the description of the electronic structure of the ground state model and experiments.

[1] R. J. McEachern and P. Taylor, A review of the oxidation of uranium dioxide at temperatures below 400 °C, J. Nucl. Mater. **254**, 87 (1998).

[2] I. Grenthe, J. Drożdżynński, T. Fujino, E. C. Buck, T. E. Albrecht-Schmitt, and S. F. Wolf, Uranium, in *The Chemistry of the Actinide and Transactinide Elements*, edited by L. R. Morss, N. M. Edelstein, and J. Fuger (Springer, Dordrecht, 2008), Vol. 1, pp. 253–698.

[3] C. Guéneau, A. Chartier, and L. Van Brutzel, Thermodynamic and thermophysical properties of the actinide oxides, in

Comprehensive Nuclear Materials, edited by R. J. M. Konings, T. R. Allen, R. E. Stoller, and S. Yamanaka (Elsevier, Oxford, UK, 2012), Vol. 2, pp. 21–59.

[4] T. Ogata, Metal fuel, in *Comprehensive Nuclear Materials*, edited by R. J. M. Konings, T. R. Allen, R. E. Stoller, and S. Yamanaka (Elsevier, Oxford, UK, 2012), Vol. 3, pp. 1–40.

[5] C. A. Colmenares, Oxidation mechanisms and catalytic properties of the actinides, Prog. Solid State Chem. **15**, 257 (1984).

[6] G. Rousseau, L. Desgranges, F. Charlot, N. Millot, J. C. Nièpce, M. Pijolat, F. Valdivieso, G. Baldinozzi, and J. F. Bérar, A

detailed study of UO_2 to U_3O_8 oxidation phases and the associated rate-limiting steps, J. Nucl. Mater. **355**, 10 (2006).

[7] L. Desgranges, G. Baldinozzi, G. Rousseau, J.-C. Nièpce, and G. Calvarin, Neutron diffraction study of the *in situ* oxidation of UO_2, Inorg. Chem. **48**, 7585 (2009).

[8] G. Leinders, J. Pakarinen, R. Delville, T. Cardinaels, K. Binnemans, and M. Verwerft, Low-temperature oxidation of fine UO_2 powders: A process of nanosized domain development, Inorg. Chem. **55**, 3915 (2016).

[9] A. M. Olsen, I. J. Schwerdt, B. Richards, and L. W. McDonald IV, Quantification of high temperature oxidation of U_3O_8 and UO_2, J. Nucl. Mater. **508**, 574 (2018).

[10] E. De Bona, K. Popa, O. Walter, M. Cologna, C. Hennig, A. C. Scheinost, and D. Prieur, Oxidation of micro- and nanograined UO_2 pellets by in situ synchrotron x-ray diffraction, Inorg. Chem. **61**, 1843 (2022).

[11] M. Magnuson, S. M. Butorin, L. Werme, J. Nordgren, K. E. Ivanov, J.-H. Guo, and D. K. Shuh, Uranium oxides investigated by x-ray absorption and emission spectroscopies, Appl. Surf. Sci. **252**, 5615 (2006).

[12] K. O. Kvashnina, P. M. Kowalski, S. M. Butorin, G. Leinders, J. Pakarinen, R. Bes, H. Li, and M. Verwerft, Trends in the valence band electronic structures of mixed uranium oxides, Chem. Commun. **54**, 9757 (2018).

[13] R. Bes, G. Leinders, and K. Kvashnina, Application of multi-edge HERFD-XAS to assess the uranium valence electronic structure in potassium uranate (KUO_3), J. Synchrotron Radiat. **29**, 21 (2022).

[14] B. O. Loopstra, Neutron diffraction investigation of U_3O_8, Acta Crystallogr. **17**, 651 (1964).

[15] A. M. George and M. D. Karkhanavala, Studies of the electrical properties of uranium oxides—I: Electrical conductivity of α-U_3O_8, J. Phys. Chem. Solids **24**, 1207 (1963).

[16] H. He, D. A. Andersson, D. D. Allred, and K. D. Rector, Determination of the insulation gap of uranium oxides by spectroscopic ellipsometry and density functional theory, J. Phys. Chem. C **117**, 16540 (2013).

[17] K. O. Kvashnina, S. M. Butorin, P. Martin, and P. Glatzel, Chemical State of Complex Uranium Oxides, Phys. Rev. Lett. **111**, 253002 (2013).

[18] G. Leinders, R. Bes, J. Pakarinen, K. Kvashnina, and M. Verwerft, Evolution of the uranium chemical state in mixed-valence oxides, Inorg. Chem. **56**, 6784 (2017).

[19] E. Enriquez, G. Wang, Y. Sharma, I. Sarpkaya, Q. Wang, D. Chen, N. Winner, X. Guo, J. Dunwoody, J. White, A. Nelson, H. Xu, P. Dowden, E. Batista, H. Htoon, P. Yang, Q. Jia, and A. Chen, Structural and optical properties of phase-pure UO_2, α-U_3O_8, and α-UO_3 epitaxial thin films grown by pulsed laser deposition, ACS Appl. Mater. Interfaces **12**, 35232 (2020).

[20] J. I. Ranasinghe, L. Malakkal, E. Jossou, B. Szpunar, and J. A. Szpunar, Comprehensive study on the electronic and optical properties of α-U_3O_8, Comput. Mater. Sci. **171**, 109264 (2020).

[21] Y. Yun, J. Rusz, M.-T. Suzuki, and P. M. Oppeneer, First-principles investigation of higher oxides of uranium and neptunium: U_3O_8 and Np_2O_5, Phys. Rev. B **83**, 075109 (2011).

[22] X.-D. Wen, R. L. Martin, G. E. Scuseria, S. P. Rudin, E. R. Batista, and A. K. Burrell, Screened hybrid and DFT + U studies of the structural, electronic, and optical properties of U_3O_8, J. Phys.: Condens. Matter **25**, 025501 (2013).

[23] N. A. Brincat, S. C. Parker, M. Molinari, G. C. Allen, and M. T. Storr, Density functional theory investigation of the layered uranium oxides U_3O_8 and U_2O_5, Dalton Trans. **44**, 2613 (2015).

[24] S. B. Isbill, A. E. Shields, J. L. Niedziela, and A. J. Miskowiec, Density functional theory investigations into the magnetic ordering of U_3O_8, Phys. Rev. Mater. **6**, 104409 (2022).

[25] W. Witczak-Krempa, G. Chen, Y. B. Kim, and L. Balents, Correlated quantum phenomena in the strong spin-orbit regime, Annu. Rev. Condens. Matter Phys. **5**, 57 (2014).

[26] J. G. Rau and M. P. J. Gingras, Frustration and anisotropic exchange in ytterbium magnets with edge-shared octahedra, Phys. Rev. B **98**, 054408 (2018).

[27] A. Miskowiec, T. Spano, Z. E. Brubaker, J. L. Niedziela, D. L. Abernathy, R. D. Hunt, and S. Finkeldei, Antiferromagnetic ordering and possible lattice response to dynamic uranium valence in U_3O_8, Phys. Rev. B **103**, 205101 (2021).

[28] E. F. Westrum, Jr. and F. Grønvold, Low temperature heat capacity and thermodynamic functions of triuranium octoxide, J. Am. Chem. Soc. **81**, 1777 (1959).

[29] M. J. M. Leask, L. E. J. Roberts, A. J. Walter, and W. P. Wolf, Low-temperature magnetic properties of some uranium oxides, J. Chem. Soc. **1963**, 4788 (1963).

[30] G. Kresse and J. Furthmüller, Efficient iterative schemes for *ab initio* total-energy calculations using a plane-wave basis set, Phys. Rev. B **54**, 11169 (1996).

[31] G. Kresse and D. Joubert, From ultrasoft pseudopotentials to the projector augmented-wave method, Phys. Rev. B **59**, 1758 (1999).

[32] S. L. Dudarev, D. Nguyen Manh, and A. P. Sutton, Effect of Mott-Hubbard correlations on the electronic structure and structural stability of uranium dioxide, Philos. Mag. B **75**, 613 (1997).

[33] G. Leinders, G. Baldinozzi, C. Ritter, R. Saniz, I. Arts, D. Lamoen, and M. Verwerft, Charge localization and magnetic correlations in the refined structure of U_3O_7, Inorg. Chem. **60**, 10550 (2021).

[34] *GW* calculations are based on an approximation to the self-energy in terms of the Green's function and the screened Coulomb interaction.

[35] M. Shishkin, M. Marsman, and G. Kresse, Accurate Quasiparticle Spectra from Self-Consistent *GW* Calculations with Vertex Corrections, Phys. Rev. Lett. **99**, 246403 (2007).

[36] https://www.vasp.at/wiki/index.php/LOPTICS.

[37] W. Setyawan and S. Curtarolo, High-throughput electronic band structure calculations: Challenges and tools, Comput. Mater. Sci. **49**, 299 (2010).

[38] See Supplemental Material at http://link.aps.org/supplemental/10.1103/PhysRevMaterials.7.054410 for the plots and discussions mentioned here and henceforth in the text.

[39] D. B. Litvin, Tables of crystallographic properties of magnetic space groups, Acta Crystallogr., Sect. A: Found. Crystallogr. **64**, 419 (2008).

[40] So far there are no reported experimental values to compare with, unfortunately.

[41] www.vasp.at/wiki.

[42] J. Even, L. Pedesseau, J.-M. Jancu, and C. Katan, Importance of spin-orbit coupling in hybrid organic/inorganic perovskites for photovoltaic applications, J. Phys. Chem. Lett. **4**, 2999 (2013).

[43] R. F. W. Bader, *Atoms in Molecules: A Quantum Theory* (Clarendon Press, Oxford, UK, 1994).

[44] P. Bultinck, C. Van Alsenoy, P. W. Ayers, and R. Carbó-Dorca, Critical analysis and extension of the Hirshfeld atoms in molecules, J. Chem. Phys. **126**, 144111 (2007).

[45] R. F. W. Bader, The quantum mechanical basis of conceptual chemistry, Monatsh. Chem. **136**, 819 (2005).

[46] B. Ao, R. Qiu, J. Tang, and J. Chen, New theoretical insights into the actual oxidation states of uranium in the solid-state compounds, J. Nucl. Mater. **543**, 152563 (2021).

[47] P. W. Anderson, Theory of magnetic exchange interactions: Exchange in insulators and semiconductors, Solid State Phys. **14**, 99 (1963).

[48] J. B. Goodenough, *Magnetism and the Chemical Bond* (Wiley, New York, 1976).

[49] J. Kanamori, Superexchange interaction and symmetry properties of electron orbitals, J. Phys. Chem. Solids **10**, 87 (1959).

[50] See Figs. 3–5 in Ref. [16]. The main difference between our results and those of He and co-workers is the strength of the second absorption peak, which shows a relatively steeper increase in their results. This may be due to the following. Our results indicate that U_3O_8 itself gives rise to a second absorption edge starting below $\sim$3 eV. If the band gap of UO_3 is 2.61 eV, as indicated in Ref. [16], then the second absorption absorption edge will be steeper in their experiment due to the combined contribution of U_3O_8 and UO_3.

[51] A caveat is appropriate here: The Tauc approximation in principle assumes parabolic bands, while in the case of U_3O_8 the bands around the conduction band minimum are flat [see Fig. S2(a)].

[52] In Refs. [19,20] the optical spectra are interpreted in the same way, with similar Tauc plots resulting in proposed band gap values close to those in Ref. [16].

Supplemental material for "Charge order, frustration relief, and spin-orbit coupling in U_3O_8"

Rolando Saniz

CMT & NANOlab Center of Excellence, Department of Physics,

University of Antwerp, B-2020 Antwerp, Belgium[*]

Gianguido Baldinozzi

Université Paris-Saclay, CentraleSupélec,

CNRS, SPMS, 91190 Gif-sur-Yvette, France[†]

Ine Arts and Dirk Lamoen

EMAT & NANOlab Center of Excellence, Department of Physics,

University of Antwerp, B-2020 Antwerp, Belgium

Gregory Leinders and Marc Verwerft

Belgian Nuclear Research Centre (SCK CEN),

Institute for Nuclear Materials Science, B-2400 Mol, Belgium

(Dated: May 15, 2023)

———

[*] rolando.saniz@uantwerpen.be

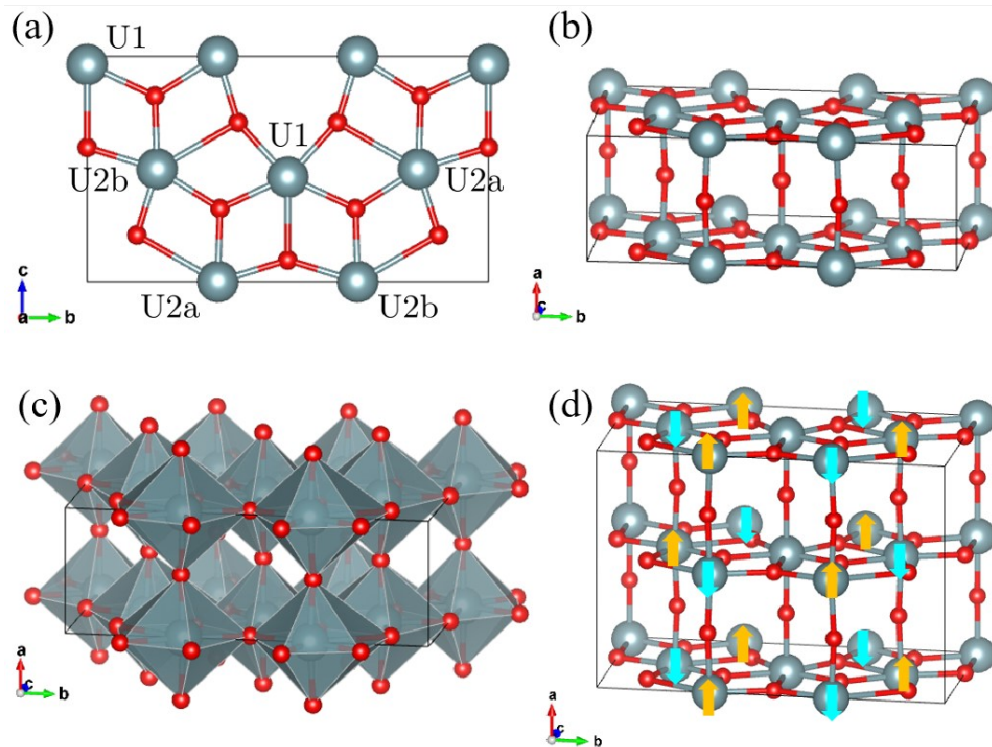[†] gianguido.baldinozzi@centralesupelec.fr

I. UNIT CELL

FIG. S1. Low temperature structure of U_3O_8. (a) Top view of the $Amm2$ orthorhombic cell. The U atom labels are for reference in the text. (b) Perspective view of the same cell, showing the layered character of the structure. (c) The oxygen pentagonal bipyramids coordinating the U atoms. (d) The $A_{2a}mm2$ unit cell, with the magnetic moments depicted, gold for the up pointing moments and cyan for the down pointing.

II. SYMMETRY AND MAGNETIC ORDER

The analysis of the symmetry of the non-magnetic structure of U_3O_8 can help understanding the changes occurring below T_N and effectively producing the compatible low temperature daughter structures. The onset of the antiferromagnetic order can be understood in terms of the symmetry adapted order parameter belonging to one of the irreducible representations of the parent space-group symmetry. The physical order parameters describing the changes (in this case, the magnetic moments) can be classified as basis functions of the irreducible representations of the parent symmetry group. In the current case, the order parameter can belong to four different magnetic irreducible representations of a single branch of the $\mathbf{q}_Z$ vector at the boundary of the parent nonmagnetic Brillouin zone $(mZ_1, mZ_2, mZ_3, or\, mZ_4)$: the individual degrees of freedom provided by an instance of these order parameters are physically meaningful because they provide a natural description of the organization of the magnetic moments in each possible daughter structure.

Indeed, lowering the temperature, some of the symmetry elements of the symmetry group of the parent phase are lost, but the surviving symmetries that describe the daughter phase are a subgroup of the parent phase that is uniquely identified by its combination with the new superlattice basis (and this eventually involves a new supercell origin choice). Borrowing from a frozen-perturbation picture, the parameters describing the low temperature daughter structures can be organized as a single polarization vector containing the cartesian components of the magnetic moments of each one of the independent U atoms of the daughter phase.
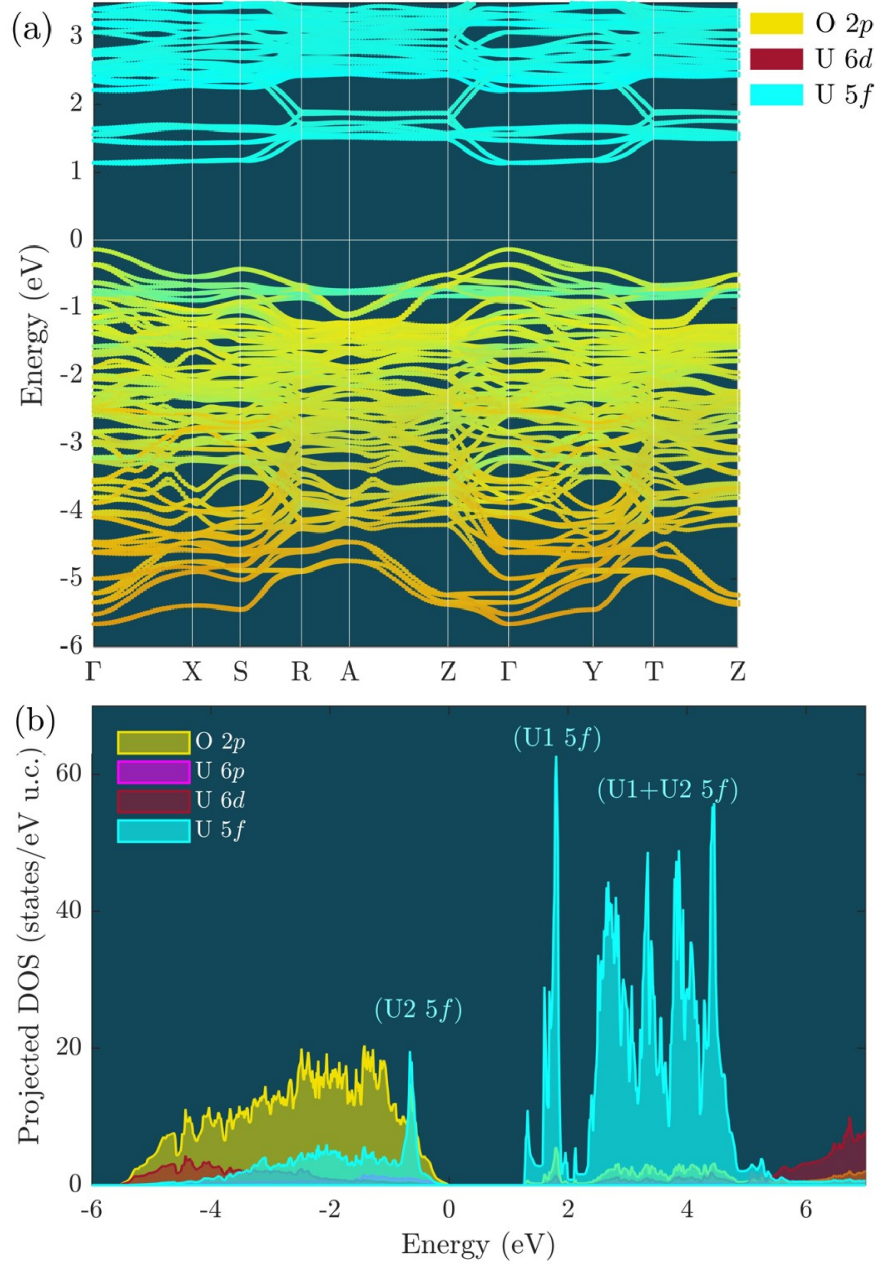
III. ELECTRONIC STRUCTURE

FIG. S2. (a) Band structure of U_3O_8, with the colors highlighting the contributions of the U $5f$, O $2p$, and U $6d$ states, which are the main contributors in the energy range shown [the valence band maximum (VBM) is at 0]. The **k**-point path used is shown in Fig. S3. (b) Atom-type projected density of states. The density of states calculations indicate that the band gap is close to 1.27 eV. The U1 and U2 $5f$ labels are for reference in the main text.
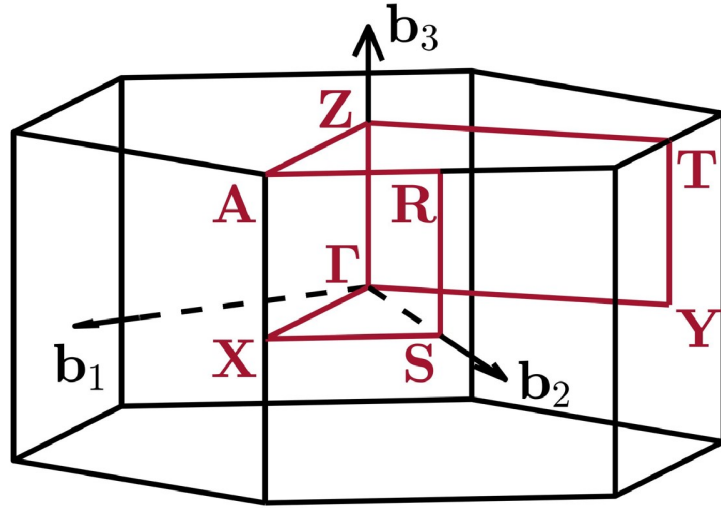
FIG. S3. **k**-point path for the band plot in Fig. S2(a). Note that we use the $C2mm$ setting of the orthorhombic cell (see Fig. 12 in Ref. 1).

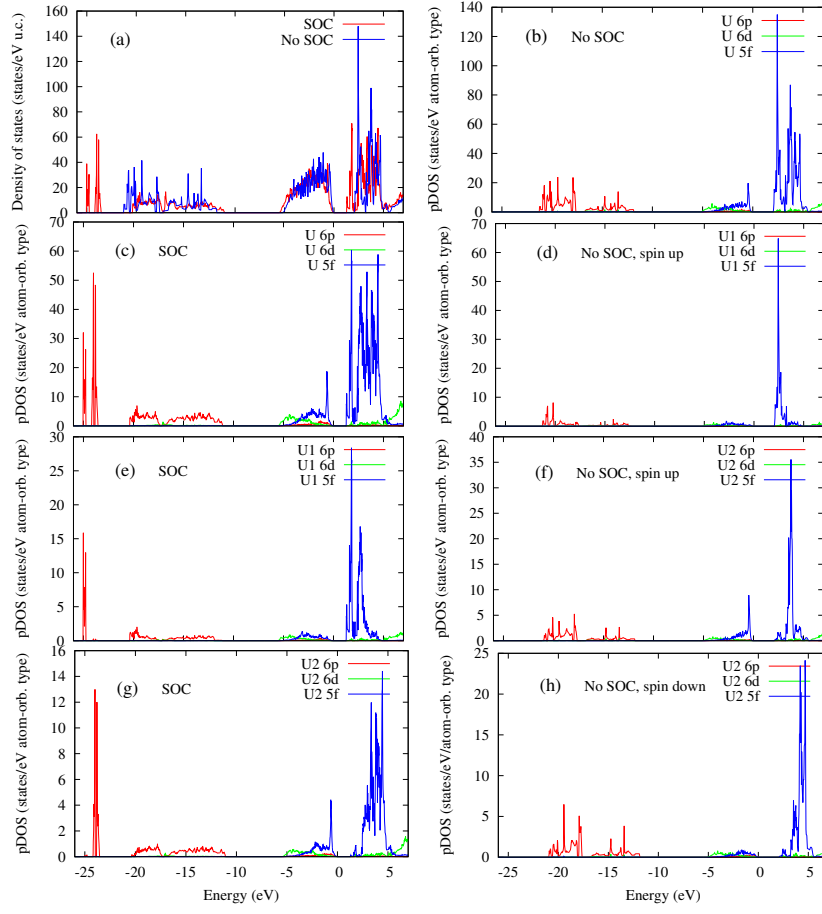# IV. PROJECTED DENSITIES OF STATES

FIG. S4. (a) Expanded views of the DOS with vs. DOS without SOC (VBM at 0). (a) SOC increases the width of the conduction and lower valence bands. The latter presents a conspicuous split induced by SOC. The nature of the states strongly affected by SOC is made clear in (b) and (c). Figures (d) and (e) compare specifically the contributions of atom U1. SOC lowers the $5f$ conduction band manifold with respect to the VBM, while increasing the band width. Also, SOC gives rise to a U1 $6p$ narrow, strong peak at ~ -25 eV. [(d) presents only the spin up DOS, as up and down states are degenerate). Figures (f), (g), and (h) compare the contribution of the U2 atoms. Figures (f) and (h) show that the magnetization is essentially due to the $5f$ states just below the VBM. Figure (g) shows that the second narrow, strong U $6p$ peak, just above -25 eV, is due to the U2 atoms. The $6p$ states (from U1 and U2) contribute to lower considerably the total energy of the system respect to a calculation neglecting SOC.
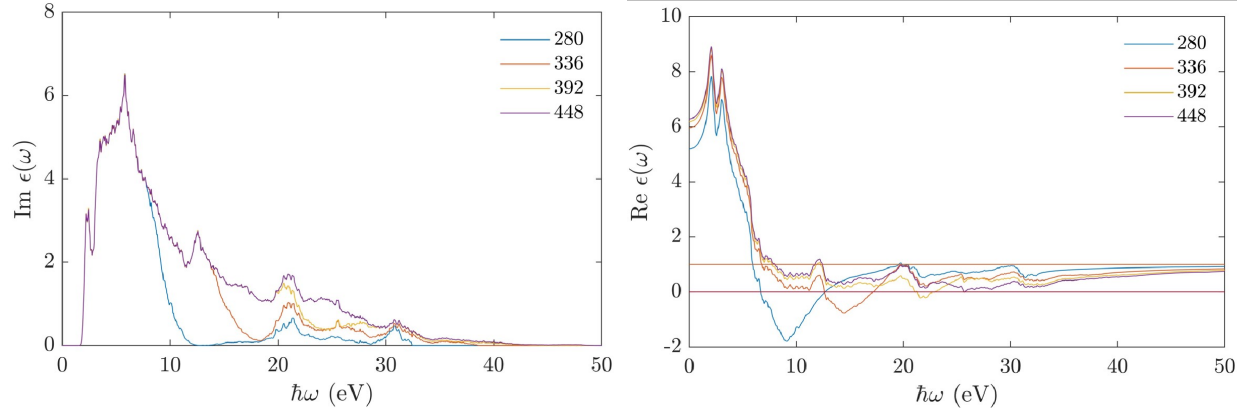
6

V. DIELECTRIC FUNCTION

FIG. S5. Imaginary part (left panel) and real part (right panel) of the dielectric function. Here the imaginary and real parts of the $\epsilon(\omega) = \text{Tr}(\varepsilon(\omega))/3$ are plotted, where ε represents the dielectric tensor. Convergence of the real part is more difficult because it is calculated based on the imaginary part, using the Kramers-Kronig relations [2]. For the real part to be converged up to a certain energy, sufficient bands should be included. Here convergence is reasonable up to 5–6 eV with 448 bands.

[1] W. Setyawan and S. Curtarolo, Comp. Mater. Sci. 49, 299 (2010).

[2] https://www.vasp.at/wiki/index.php/LOPTICS